Influence of Induced Electron Yields of Ubiquitous Materials on Absolute Charging of GSAT-19

Keyurkumar Patel¹, Rizwan Alad², Ashish Pandya³, and Suryakant Gupta⁴

^{1,2,3}Department of Electronics & Communication, Dharmsinh Desai University, Nadiad, Gujarat 387001, India.

⁴Institute of Plasma Research, Gandhinagar - Ahmedabad Rd, GIDC Bhat, Bhat, Ahmedabad, Gujarat 382428, India.

Abstract

Space plasma particles and space weather conditions strongly affect spacecraft at Geosynchronous Earth Orbit (GEO). Their charging primarily occurs due to incoming primary electrons and outgoing secondary and backscattered electrons. This study endeavours to quantify the absolute charging resulting from the impact of induced electron yields (secondary electronsand backscattered electrons) on the surfaces of the GSAT-19 satellite. The GSAT-19 is depicted as a structure composed of a metallic cuboid featuring two co-planar plates, parabolic reflector antennas, and an offset parabolic antenna. The most influential factors for the computation of absolute charging are the varying yields values of SE and BE associated with different materials. To precisely evaluate the time-dependent behavior of body potential on the satellite, We have calculated the capacitance accurately through the MomentsMethod. This study specifically explores the consequence of the normal incidence of particles on Aluminum(Al) and Copper-Beryllium(Cu-Be) metal surfaces, during both normal-case and worst-case scenarios duringsingle Maxwellian plasma environment. This analysis provides a reliable prediction of ESD threat for Al and Cu-Be metal surfaces through its absolute charging.

Keywords: Backscattered Electrons(BE), Electrostatic Discharge (ESD), GSAT (Geosynchronous Satellite), Secondary Electron (SE)

1.Introduction

Spacecraft charging happens when charged particles from the surrounding energetic charged particles environment accumulate on the spacecraft. This can occur on the surface, interior parts, dielectrics, or conductors. A spacecraft acts as a Langmuir probe in the space plasma environment. Like any electrical probe in the plasma, it accumulates charge and assumes an electrostatic potential consistent with charge collection, as dictated by Maxwell's equations[1-2]. This collection of charge from the environment is known as spacecraft charging, which can be categorized as deep dielectric charging, absolute charging, and differential charging. All of these pose a serious risk to the spacecraft. Highly energetic ambient electrons and ions (ranging from 0.1 MeV to 3 MeV for GEO orbits) are responsible for deep dielectric charging, while energy in the range of upto 50 keV is accountable for surface (differential and absolute) charging[3]. These surface charging affects the space operations.

To ensure the long-term reliability of space operations, it is crucial to assess the influence of key space environment elements such as the macroscopic particles, plasma, geomagnetic field, neutral atmosphere, radiation, temperature field, and solar activities on spacecraft charging. Research on spacecraft charging is necessary as approximately 40% of total anomalies are attributed to the space environment [4]. The plasma, consisting mainly of ions and electrons constitutes approximately 99% of cosmic substances [5] and it influences spacecraft charging under both cold and hot plasma conditions. Additionally, electromagnetic radiation (EM) originating from the solar disk and other

terrestrial systems affects the exposed satellite bodies, resulting in spacecraft charging [4],[6]. The result of a particle impact is contingent upon the incident energy level, predominantly resulting in either deep dielectric charging or surface charging. Deep dielectric charging, presenting a threat to onboard electronics, occurs infrequently owing to the diminished presence of high-energy charged particles (0.1-3 MeV for GEO orbit) in space. Conversely, surface charging is predominantly instigated by charged particles possessing energies within the range of up to 50 keV in the space environment[7-9]. When a primary charged particle strikes a surface, there is a possibility of backscattering or secondary electrons from the surface. Secondary and backscattered electrons depend on the material characteristics of the surface, the particle energy and angle of incidence [2]. The influences of outgoing electron yields of widely used spacecraft material, Cu-be and Al on absolute charging of GSAT19 are presented in this paper.

2.Literature Rivew

The study of charging on spacecraft has been facilitated by the utilization of various available tools, including NASA Charging Analyzer Program (NASCAP-2K)[10], Multi-utility Spacecraft Charging Analysis Tool (MUSCAT)[11], Spacecraft Plasma Interaction Software (SPIS) [12,13] and PTetra[14]. NASCAP-2K[10] employs the boundary element method as its computational approach. MUSCAT[11] can determine the time-dependent behavior of spacecraft potential based on given plasma conditions. MUSCAT [11] was used to analyze charging for huge satellites at GEO. The specific numerical methods employed by MUSCAT is not disclosed in detail. On the contrary, the SPIS software[12,13] excels in computing spacecraft potential, taking into account of various factors such as secondary emission, back-scattering electrons, photo-emission, sheath, and other relevant parameters. This software tool utilizes the finite-element method for its operations. In a distinct investigation [14], the PTetra tool was employed for calculating coupling capacitanceof spacecraftsurfaces. PTetra employs the finite-element Taylor-Galerking numerical method with linear interpolation functions. Recently spacecraft charging is also analyzed using EMA3D Charge tool [15]. It is based on the finite element method (FEM) for internal charging and the boundary element method (BEM) for surface charging.

Apart from the works which have been presented using tools, recently, spacecraft charging have been reported using some experimental and numerical method. Spacecraft charging has been analyzed numerically and analytically using Whittaker function. Numerical analysis of spacecraft charging has been carried out for aluminum and silver. However, This work did not consider the surface changing analysis for Cu-Be material [16]. Spacecraft charging within GEO is analyzed using the helium oxygen proton electron and electric field and wavesinstruments from the Van Allen Probes. this study explored how spacecraft potential relates to electron number density, electron pressure, electron temperature, thermal electron current, and low-energy ion density between 1 and 210 eV [17]. The fast active charging effect of spacecraft is observed under the action of plasma contactors in the GEO orbit by using a two-dimensional Particle-in-Cell model [18]. The analysis on variations in temporal profile of body potential and electrostatic discharge (ESD) becomes exceedingly untrustworthy without the knowledge of the capacitance of satellite. The worksdiscussed in the above literatures did not reveal the capacitance of the satellite and its various structures. In view of these, we referred the following literature which provides a detailed methodology for capacitance computation as well as the surface charging. Previously, studies on spacecraft charging have focused on modeling spacecraft as a sphere, as reported in [19-21]. In [22-25], The capacitance and time-dependent behavior of body potential profiles of individual spacecraft components and entire satellite (GSAT-14), were simulated by modeling them as rectangular cuboids featuring two plates and antennas. Nevertheless, these analyses have not discussed the influence of SEand BE [22-25]. A recent study has examined the surface charging of GSAT-19 during a sunlit-eclipse-sunlit passage, considering the worst-case environmental conditions and utilizing the single Maxwellian plasma model [26]. This study did not incorporate the effect of angle of incidence which is crucial for the determination of electron yields and subsequently charging. Furthermore, another investigation in [27] presents the influence of secondary and back-scattered electrons on the surface charging of metallic pyramids with a cuboid structure commonly employed in spacecraft. Subsequently, The work in [28], presented the assessment of the differential charging occurring at the triple junction of spacecraft, specifically caused by the secondary and back-scattered electron currents at adjacent dissimilar material surfaces.

The primary electrons originating from the space plasma interact with the surface material, inciting secondary electron excitement from the material or reflecting (back-scattering) the same electrons. Additionally, ions impacting the surface can induce SE[29,30]. The significance of electron yields becomes apparent in establishing the quantity of electrons emitted from a material surface. The magnitudes of these yields are affected by the energy and incident trajectory angle of primary particles. The large numbers of outgoing electrons results in the surface floating at additional positive potential. Therefore, it is crucial to consider the SE-BE characteristics of various material surfaces to accurately estimate surface charging.

The existing literature lacks a report on the body capacitance and transient variation of potential on the body of the GSAT-19 spacecraft. This analysis specifically focuses on the effect of the angle of incidence in worst-case and normal-case space plasma conditions for single Maxwellian plasma models, considering material properties and primarily incorporating recognized SE-BE formulations.

The work presented in this paper is organized as follows. Section 3 presents methodology for the computation of capacitance and body potential. The body capacitance of GSAT-19 is computed using the Moments Method [31]. The body potential on surface material is computed in single Maxwellian plasma environment for normal and worst cases for the normal incidence. The materials most commonly used in satellites, listed in [32], include Al and Cu-Be, which are considered in this study. Section 4 encompasses the numerical results and discussion which provides the detailed study on ESD events based on the time-dependent behavior of the body potential profile of GSAT-19. We equated our charging results with earlierreported results of GSAT-14[22]to confirm our methodology. The results of the impact of variation of induced electron yields of Cu-Be and Al under both normal and worst-case single Maxwellian plasma environments are presented. Finally, concluding remarks and future extension of this work are also covered in section 5.

3.Methods

The structure of the GSAT-19, illustrated in Fig. 1 comprises a metal cuboid and rectangular plates that depict photovoltaic panels, parabolic reflectors (offset), and a primary reflector antenna. Furthermore, photovoltaic panel (solar panels) are affixed to the back and front sides of the metal cuboid via a yoke. The middle point of the metal cuboid serves as the point of origin in the coordinate system. In the XZ plane, the spin angle of the photovoltaic panel is defined around the Z-axis θ =0°. The parabolic reflector antenna is positioned at the upper surface of the cuboid. Two reflector antennas (parabolic) are attached to both sides of the cuboid (YZ plane). The photovoltaic panel are oriented co-planer to the XZ plane.

Moments Method formulation is shownin Section 3.1 for the numerical computation of capacitance of GSAT-19. Section 3.2 presents the mathematical formulation to estimate the time-dependent behavior to reach a steady-state value of body potential. In order to recognize the contribution of SE-BE, We have considered two cases of absolute charging. In first case, the body potential is achieved by considering primary currents of electrons and ions only. Subsequently, charging analysis is conducted with involvement of currents induced by SE and BE also.

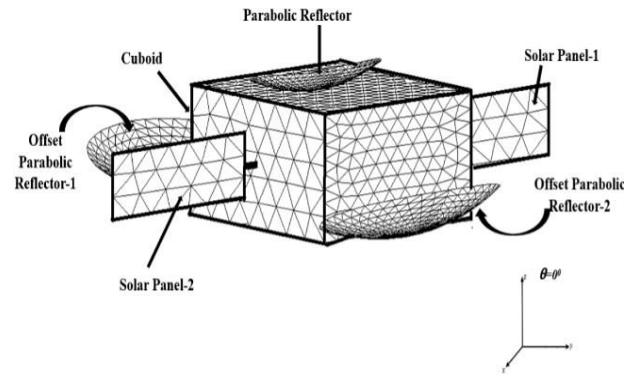


Figure 1. GSAT-19 configuration for electrostatic analysis using MoM

3.1 Evaluation of capacitance

To determine the capacitance, the structure is divided into triangular meshes, as illustrated in Figure 1. The unspecified density of charge on the structure at a specific point d'(x',y',z') is denoted as $\sigma(d')$. The potential at any random point d(x,y,z) is represented as

$$V(d) = \frac{1}{4\pi\epsilon_0} \int_{S} \frac{\sigma(d')}{|d-d'|} dS$$
 [1]

All structures are treated as perfect conductors, assuming they form equipotential surfaces. Thesurface mentioned in equation (1) corresponds to different body parts of the spacecraft, namely the metallic cuboid S_1 , two solar panels S_2 and S_3 main parabolic reflector S_4 , and two offset parabolic reflectors S_5 and S_6 . The unspecified charge distributions on these surfaces are represented by σ_i while V_i denotes the potentials corresponding to surfaces where i=1,2,3,4,5,6. In the current scenario, the potentials are interpreted relative to the nearby plasma potential, with the bodies of spacecraft expected to be perfect conductors, where $V_1 = V_2 = V_3 = V_4 = V_5 = V_6 = V$. Hence, the potential V_1 on the metal cuboid can be expressed as equation (2),

$$V_{1} = \frac{1}{4\pi\varepsilon_{0}} \left[\underbrace{\int_{S_{1}} \frac{\sigma_{I}(d_{I}')}{|d_{I}-d_{I}'|} dS_{1}}_{V_{11}} + \dots + \underbrace{\int_{S_{1}} \frac{\sigma_{6}(d_{6}')}{|d_{6}-d_{6}'|} dS_{6}}_{V_{16}} \right]$$
[2]

The potential V_{11} corresponds to the potential on the metal cuboid resulting from its charges. while V_{1i} represents the potentials resulting from the charges distributed on the surface of other bodies, namely S_i , Where i=2,3,4,5,6. The vectors of position d_i ' denote the source points on the surface of other bodies, Likewise, the potential V_i on the remaining five geometries can be expressed, giving rise to five integral equations involving five unknowns, namely σ_i , where i=2,3,4,5,6. The unspecified charge distributions on surfaces σ_i are determined by solving equations using MoM. To implement the MoM, each of the six bodies is subdivided into several triangular subsections. The unspecified charge distributions are written in terms of pulse basis functions as follows,

$$\sigma(d) = \sum_{i=1}^{N} \alpha_n f_n$$
 [3]

In the equations f_n represents the pulse basis functions, α_n denotes the unknown surface charge coefficient per unit area of the body surface being analyzed, and n represents the triangular subsection's number. To obtain the group simultaneous equations, equation (3) is substituted into equation (2) using the point matching method and the Dirac delta function as the testing function. The resultant six linear equations can be resolved through the Generalized Minimal Residual Method (GMRES) technique [33]. This method is utilized to calculate the unspecified charge density of each conducting body surface. Subsequently, the unspecified charge on body surface can be found by equation (4),

$$Q_{j} = \sum_{n=1}^{N_{j}} \alpha_{1n} A_{i}$$
 [4]

Where N_j is the number of triangular subsections of body parts, j=1 to 6, i=1 to 6 and A_1 , A_2 , A_3 , A_4 , A_5 , and A_6 are the area of the body parts of spacecraft. The net charge of the bodyof the spacecraft is the addition of the charges on each part of the spacecraft. The free space capacitance concerning infinity can be expressed using equation (5),

$$C_{body} = \frac{\sum_{i=1}^{6} Q_i}{V}$$
 [5]

3.2 Evaluation of spacecraft body potential

The spacecraft's body potential is calculated based on the spacecraft model illustrated in Fig. 1. The primarysources of current, specifically the density of the electron current (J_e) and density of ion current (J_i) are acknowledged as the principal contributors. The net current density directed toward the spacecraft is established in [34]. The balance current for the spacecraft surface potential $V_s < 0$ is as follows in equation (6),

$$J_{net} = -J_{oe} \exp\left(\frac{\text{eV}_s}{\text{k}T_e}\right) + J_{oi} \exp\left(1 - \frac{\text{eV}_s}{\text{k}T_i}\right) + J_{se} + J_{be} + J_{si}$$
Where, $J_{oe,i} = Kn_{e,i} \sqrt{\frac{\text{k}T_{e,i}}{\text{m}_{e,i}}}$ and $V_s < 0$

In this context, the factor $K = \frac{1}{\sqrt{2\pi}}$ and k is the Boltzmann constant. Vs is potential on the surface relative to the space plasma, with the assumption that the space plasma potential is zero. J_{net} denotes the overall current density arising from the space plasma. J_e and J_i correspond to the current density of environmental incident electrons and ions, respectively. J_{se} and J_{be} denote the current density of secondary emitted electrons and back-scattered electrons respectively. J_{si} specifically represents the ion-induced secondary emitted electron current density. $T_{e,i}$, $m_{e,i}$, and $n_{e,I}$ represent temperature, mass, and the density of electrons and ions, respectively. J_{oe} and J_{oi} denote the current density of electrons and ions relative to plasma potential.

By employing the required expressions of J_{se} and J_{be} along with energy distribution function(single Maxwellian distribution), the equation (6) is solved. Density of secondary electron current due to electrons J_{se} is denoted as [30],

$$J_{se} = e\left(\frac{2\pi}{m_e^2}\right) \int_0^\infty Y_{se}(E) E f(E) dE \exp\left(\frac{eV_s}{kT_e}\right)$$
 [7]

Where,
$$Y_{se} = \frac{1.114\delta_{\rm m}}{\cos\theta} \left(\frac{E_m}{E}\right) \left\{ 1 - \exp\left[-2.28\cos\theta \left(\frac{E}{E_m}\right)^{1.35}\right] \right\}$$
 [8]

Here, E_m represents primary energy at the maximum yield δ_m is observed. Taking into account of the incidence angle θ of SE. Surface charging analysis for normal incidences is carried out. Equation (8) simplifies for normal incidence as follows,

$$Y_{se} = 1.114 \left[\exp(-Q) \delta_{\rm m} \left(\frac{E}{E_{\rm m}} \right)^{0.35} \right]$$
 [9]

 E_m and Y_{se} represent the energy of incident electron and energy respectively, while f(E) denotes energy distribution function (single Maxwellianplasma velocity distribution function of ambient electrons). The expression of f(E) can be found in [32],

$$f(E) = n_{\rm e} \left[\frac{m_e}{2\pi k T_{\rm e}} \right]^{\frac{3}{2}} \exp\left(\frac{-E}{k T_e} \right)$$
 where,
$$E = \frac{1}{2} m_e v_e^2$$

Where, v_e represent the velocity of the electron. The analysis is performed by employing the model proposed by Whipple for secondary electron [30]. This model is angle-dependent, with the normal incidence ($\theta = 0^{\circ}$) being utilized in the simulation. The expression for J_{si} is given by [36],

$$J_{si} = e\left(\frac{2\pi}{m_e^2}\right) \int_0^\infty Y_{si}(E - eV) E f(E) dE \exp\left(1 - \frac{eV_s}{kT_i}\right)$$
[11]

 Y_{si} is expressed for normal incidence as follows in equation (12),

$$Y_{si} = \delta_1 E^{1/2} \frac{\left(1 + \frac{1}{E_m}\right)}{\left(1 + \frac{E}{E_m}\right)}$$
 [12]

Where, δ_1 is yield at 1 keV and E_m is energy at maximum yield.

The representation for J_{be} is specified as [29]:

$$J_{be} = e\left(\frac{2\pi}{m_e^2}\right) \int_0^\infty Y_{be}(E) E f(E) dE \exp\left(\frac{eV_s}{kT_e}\right)$$
 [13]

 Y_{be} can be determined through atomic number of material (Z) and the energy of the incident electron for normal incidence using equation (14) [35],

$$Y_{be} = \begin{cases} 0.0 & ;E > 100000 \\ 1 - 0.7358^{0.037Z} & ;E = 10,000 - 100,000 \\ 1 - 0.7358^{0.037Z} + 0.1 \exp\left(\frac{E}{5000}\right); E = 1,000 - 10,000 \\ 0.3338 \ln\left(\frac{E}{50}\right) \left[1 - 1 - 0.7358^{0.037Z} + 0.1 \exp\left(\frac{E}{5000}\right)\right]; \quad E = 50 - 1,000 \\ 0.0 & ;E < 50 \end{cases}$$

The surface potential can be represented as

$$\frac{dV}{dt} = \frac{I}{C_{body}} J_{net} A$$
 [15]

The structure's surface area is denoted by A, and C_{body} represents the converged body capacitance, as discussed in Section 2.1.

The time-dependent performance of body potential is acquired by equation (15) after applying integration using the fourth-order Runge-Kutta method under two conditions as discussed in Sections 2.3 and 2.4.

3.2.1 Computing the body potential without the influence of SE-BE

Initially, we derived the body potential exclusively by taking into account of density of electron current density (J_e) and the density of ion current (J_i) . This body potential is referred to as $V_{(ZEY)}$. The equation (15) is represented as,

$$\frac{dV_{(ZEY)}}{dt} = \frac{1}{C_{body}} (-J_e + J_i) A$$
 [16]

3.2.2 Computing the body potential with the influence of SE-BE

To observe the influences of SE-BE on surface charging, The body potential is established by integrating the contributions of J_{se} , J_{be} , and J_{si} into J_e and J_e . The resultant body potential is referred to as $V_{(SE-BE)}$. The equation (15) is then given as follows

$$\frac{dV_{(SE-BE)}}{dt} = \frac{1}{C_{body}} (-J_e + J_i + J_{se} + J_{si} + J_{be})A$$
 [17]

4. Numerical result and Discussion

In section 4.1, the computation results of the capacitance of GSAT-19 and the body potential temporal profile of GSAT-19 are discussed and compared with GSAT-14 for the validation of the adopted methodology. The steady-state body potential in recommended cases of plasma is elaborated in section 4.2.

4.1 Spacecraft Capacitance and confirmation of evaluation.

The capacitance computation is performed for Figure 1 which consists of a cuboid with dimensions L x W x H of 2.010 m x 2.9 m x 1.720 m, two planar rectangular plates with dimensions L x W of 1.8 m x 0.9 m, two parabolic reflectors (offset) with an aperturediameter of 2 m, and parabolic reflectors (main) with an aperture diameter of 1 m. The computed capacitance converges to 202.61 pF using 3510 non-uniform triangular divisions. No notable variation in capacitance is observed after 3510 subsections. As noted in [22], the converged capacitance value of GSAT-14 is 221.48 pF. A comparison of the capacitance and saturation time for the GSAT-14 and GSAT-19 satellites is presented in Table 1.

Table 1 Comparison of saturation time without SE-BE at $V_{(ZEY)}$ = -19071	Table 1 Comparison	of saturation	time without	t SE-BE at $V_{\ell ZEY}$	j= -19071V
--	---------------------------	---------------	--------------	---------------------------	------------

Structures	Capacitance (pF)	Saturation time (ms)
GSAT-19	221.48	1240
GAST-14	202.61	880

To validate the adopted methodology, we estimate the steady-state body potential of the GSAT-14 and GSAT-19 spacecraft for η_e = 1.25 x 10⁶m⁻³, k T_{e} = 7.5 keV, η_i = 1.25 x 10⁶m⁻³,k T_{i} = 10 keV [21] using the converged value of capacitance. The obtained value of the spacecraft's body potential, as depicted in Figure 2 is -19071V, which closely aligns with the -19095V reported in [21,22]. Therefore, the result obtained in this paper is consistent with previous works. The GSAT-19 attains an equilibrium state of body potential at -19071 V after approximately 0.9 seconds, which is 0.3 seconds earlier than GSAT-14. The shorter time required to achieve a steady bodypotential amplitude of approximately -19 kV results in greater number of ESD events over the spacecraft's lifetime.

4.2 Evaluation of the body's potential

The GSAT-19 is taken into account to calculate the body potential for the recommended plasma scenarios, specifically the worst case and normal case. The worstcase represents an extreme condition in which the spacecraft charges with the most negative body potential. The normal case represents a quiet plasma environment. The plasma environment parameters of normal-case [37] and worst-case [38] are listed in Table 2. In this study, the spacecraft body is assumed to be fully conducting materials. Initially, the body potential is calculated for spacecraft without SE-BE currents.

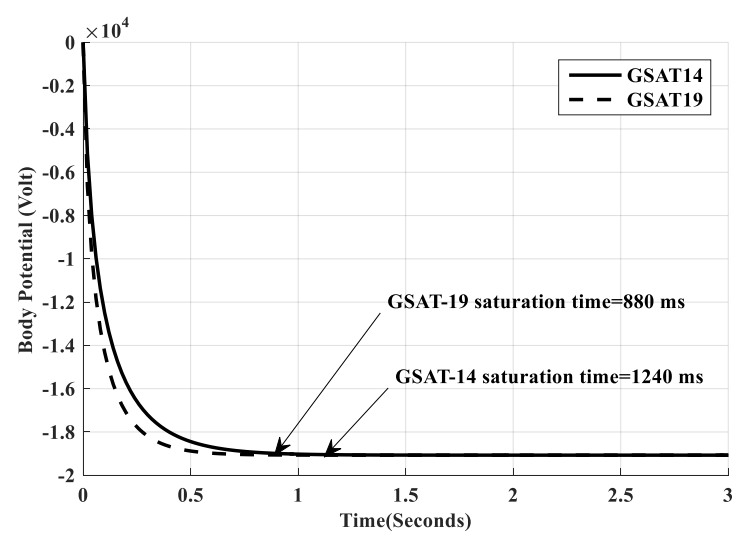


Figure 2. Comparison of temporal body profile of GSAT-19 & GSAT-14.

In the normal scenario, a body potential of -15,095 V stabilizes within 1.5 seconds, consistent with the value in [21]. Under worst-case conditions, the body potential reaches -62,969 V at 7.36 seconds, closely approximating the -62,970 V documented in [27], as illustrated in Figure 3.

Table 2 plasma	parameters	(Single	Maxwellian	plasma)	[37,	38]

Parameters	Normal	Worst	
	case	case	
(3)	1.09 x	1.2 x	
$\eta_e(\mathrm{m}^{-3})$	10^{6}	10^{6}	
kT_e (keV)	4.83	16	
(3)	580 x	236 x	
η_i (m ⁻³)	10^{6}	10^{6}	
kT_i (keV)	14.5	29.5	

Next, the body potential of frequently used spacecraft materials is examined, taking into consideration the SE-BE effect in both normal and worst-case scenarios. The electron-induced SE and ion-induced SE parameters for Cu-Be and Al are listed in Table 3 [32].

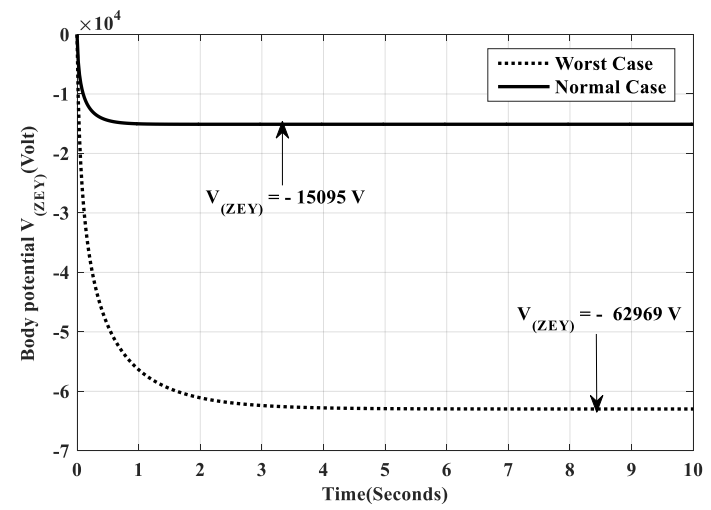


Figure 3. Time-dependent performance of body potential $V_{(ZEY)}$ in normal case & worst case of plasma

The resulting body potential, incorporating the effect of SE-BE, is obtained by integrating equation (17) and is denoted as $V_{(SE-BE)}$.

Table 3 Material Parameters [32]

Parameters	Cu-Be	Al
Incident electron peak	2.2	0.97
emission coefficient (δ_m)		
Incident electron peak energy	0.3 keV	0.3
(E_m)		keV
Incident ions emission	0.244	0.244
coefficient at $1 \text{keV}(\delta_1)$		
Ion energy at peak yield(E_m)	230 keV	230
		keV
Atomic identity number(Z)	29	13

The effect of SE-BE on the body potential of Cu-Be and Al as it varies with energy is presented in Figure 4, using the single Maxwellian plasma model at normal incidence.

In the normal case, the steady-state body potential on Cu-Be increases from -15095 V to -14706 V at 50 keV particle energy. Meanwhile, the body potential on Al reaches from -15095 V to -14927 V at the same particle energy. The difference between $V_{(ZEY)}$ and $V_{(SE-BE)}$ is 389 V and 168 V for Cu-Be and Al, respectively, at 50 keV particle energy.

Figure 5 demonstrates a positive correlation between outgoing current density $J_{\rm (SE-BE)}$ and particle energy. The positive pattern reveals the influence of current density as a result of SE-BE. The outgoing current density for Cu-Be is by 1.01×10^{-7} A/m²more than Al in the normal case which leads the surface more positive. The body potential on Cu-Be and Al, along with the net outgoing current density, are depicted for worst case in Figure 6 and Figure 7respectively. The steady-state body potential on Cu-Be reaches -62228 V at 50 keV particle energy, which is 741 V more than the -62969 V in the worst case.

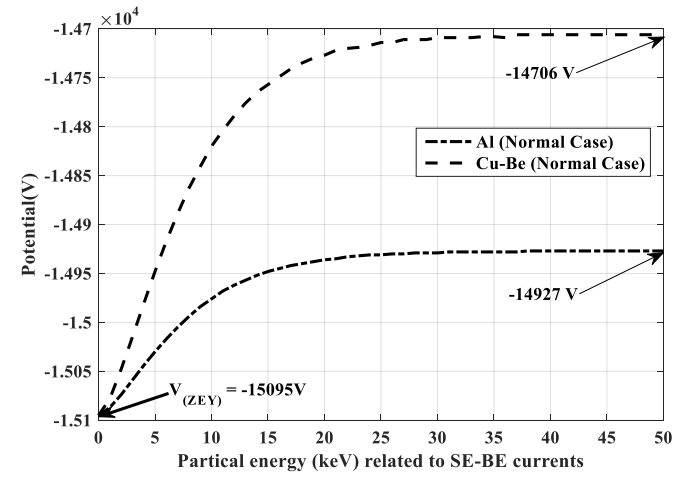


Figure 4. Body potential versus particle energy related to currents of SE-BE in normal case

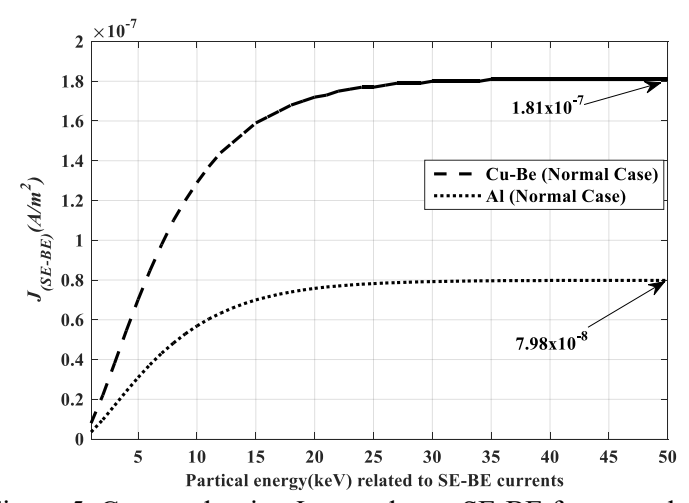


Figure 5. Current density $J_{(SE-BE)}$ due to SE-BE for normal case.

Similarly, the body potential on Al reaches -62637 V at 50 keV particle energy, which is 332 V more than the -62969 V in the worst case. There is a significant difference between $V_{(ZEY)}$ and $V_{(SE-BE)}$ in the worst case compared to the normal case.

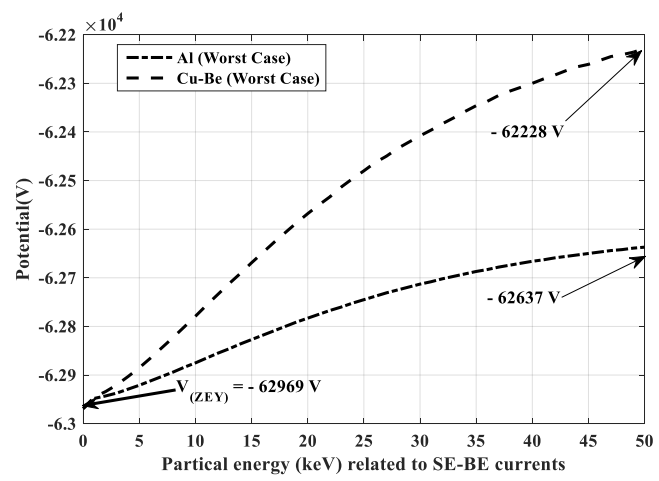


Figure 6. Body potential versus particle energy related to currents of SE-BE in worst case

In the worst case, the surface charges more positively than $V_{(ZEY)}$. This is due to the presence of higher electron yields contributed by highly energetic ions. The higher energy particles produces more total induced electron yield [27]. Accordingly, the outgoing current density for Cu-Be exceeds that of Al by 1.18 x 10^{-7} A/m². The high value of outgoing current density makes surface more positive in worst case likewise normal case. The higher electron temperature and electron-induced yield significantly affect the absolute charging behavior in the worst-case scenario.

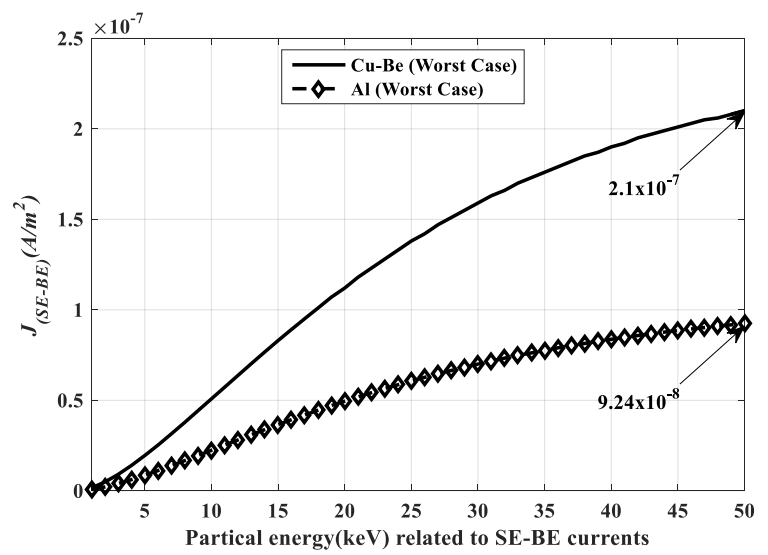


Figure 7. Current density $J_{(SE-BE)}$ due to SE-BE for the worst case

5. Conclusion and Future work

This paper shows an estimation of the absolute charging of GSAT-19, considering induced electron yields in both normal and worst-case plasma environments. The computations are based on single Maxwellian plasma parameters, and the results reveal significant positive charging concerning $V_{(ZEY)}$. The following are the major insights derived from these numerical computations.

(i) GSAT-19 attains a steady-state body potential 0.4 seconds quicker than GSAT-14, which could result in a higher number of ESD events for GSAT-19.(ii) Beyond 10 keV of particle energy, both in the normal and worst-case scenarios, there is a significant positive trend in the steady-state body potential concerning $V_{(ZEY)}$. (iiiAt an energy level of 50 keV, the steady-state potential is approximately 389 V more positive for Cu-Be in normal conditions and 741 V more positive in worst-case conditions when compared to Al. Thus, this result confirms the influence of greater induced electron yields of Cu-Be over Al on the charging of GEO satellite structures.(iv) Upon comparing the

absolute charging of spacecraft made from both materials, it becomes evident that the possibility of an ESD threat is higher in the case of Al, primarily due to its higher charging propensity. This workprovides the charging analysis in eclipse condition, and hence it does not include the impact of photoelectrons. This analysis can be enhanced by incorporating the current density of photoelectrons.

References

- [1] S. T. Lai, Fundamentals of Spacecraft Charging: Spacecraft Interactions with Space Plasmas, Princeton, NJ, USA: Princeton Univ. Press, 2012,pp.1-9.
- [2] D. E. Hastings and H. B. Garrett, Spacecraft-Environment Interactions, Cambridge, U.K.: Cambridge Univ. Press, 1996, pp. 20,146 152.
- [3] S. T. Lai, Spacecraft Charging, American Institute of Aeronautics and Astronautics, Inc., 2011, Vol. 237, pp.1-3, 87-88.
- [4] H. B. Garrett and A. C. Whittlesey, "Spacecraft charging, an update," IEEE Trans. Plasma Sci., Dec. 2000 vol. 28, no. 6, pp. 2017–2028.
- [5] E. Yigit, "Atmospheric and Space Sciences: Ionospheres and Plasma Environments," (Springer Briefs in Earth Sciences), 2017, vol. 2.
- [6] M. Cho, J. H. Kim, S. Hosoda, Y. Nozaki, T. Miura and T. Iwata, "Electrostatic Discharge Ground Test of a Polar Orbit Satellite Solar Panel," IEEE Transactions on Plasma Science, Oct. 2006, vol. 34, no. 5, pp. 2011-2030.
- [7] Garrett H, Whittlesey AC. Guide To Mitigating Spacecraft Charging Effects. Hoboken, New Jersey: John Wiley & Sons, Inc;2012,7-9.
- [8] Hastings D, Garrett H. Spacecraft-Environment Interactions. U.K: Cambridge Univ. 2012, Press; 31-32,143-144, 154-156, 162-165.
- [9] Lai ST. Fundamentals of Spacecraft Charging: Spacecraft Interactions with Space Plasmas. USA, xviii-xix: Princeton Univ. Press; 2012, 2-3, 18-23, 26-29.
- [10] M. J. Mandell, V. A. Davis, D. L. Cooke, A. T. Wheelock, and C. J. Roth, "Nascap-2k spacecraft charging code overview," IEEE Trans. Plasma Sci., Oct. 2006, vol. 34, no. 5, pp. 2084–2093.
- [11] T. Muranaka et al. "Development of multi-utility spacecraft charging analysis tool (MUSCAT)," IEEE Trans. Plasma Sci., Oct. 2008, vol. 36, no. 5, pp. 2336–2349.
- [12] J. F. Roussel, F. Rogier, D. Volpert, J. Forest, G. Rousseau, and A. Hilgers, "Spacecraft plasma interaction software (SPIS): Numerical solvers—Methods and architecture," in Proc. Apr. 2005, Process. 9th Spacecraft Charg. Technol. Conf., Tsukuba, Japan, pp. 462–472.
- [13] J.F. Roussel et al., "SPIS multi-timescale and multiphysics capabilities: Development and application to GEO charging and flashover modeling," IEEE Trans. Plasma Sci., Feb. 2012., vol. 40, no. 2, pp. 183–191.
- [14] R. Marchand, "PTetra, a tool to simulate low orbit satellite-plasma interaction," IEEE Trans. Plasma Sci., Feb. 2012, vol. 40, no. 2, pp. 217–229.
- [15] Merenda, Kevin-Druis, et al. "Spacecraft charging with EMA3D Charge." Advances in Space Research 72.12 2023,5626-5635.
- [16]Pervaiz, Fareeha, et al. "Spacecraft charging due to energetic electrons and ions at geosynchronous altitudes." Journal of Geophysical Research: Space Physics 128.1 ,2023,e2022JA030642.
- [17] Breneman, Aaron W., et al. "The Van Allen Probes electric field and waves instrument: Science results, measurements, and access to data." Space science reviews 218.8, 2022, 69
- [18] Xue, Bixi, et al. "Fast Spacecraft Charging Mitigation With Plasma Contactors During High-Power Electron Beam Emission in the GEO Environment." Journal of Geophysical Research: Space Physics 129.1,2024, e2023JA031783.
- [19] Mehta BK, Deshpande SP, Mukherjee S, Puthanveettil SE. "Differential charging calculation of spherical geometry in space plasma condition," J Spacer Technol. 2011;21(1):7-19.
- [20] ECSS document: ECSS-E-HB-20-06A, Assessment of space worst-case charging handbook, The European Cooperation for Space Standardization, 2019.
- [21] Karthikeyan B, Hariharan VK, Sanyal S., "Estimation of free space capacitance and body potential of a spacecraft for charging analysis," IEEE Trans Plasma Sci, 2013, 41(12):3487-3491.
- [22] Alad R.H, Chakrabarty SB., "Electrostatic analysis of an artificial orbiting satellite for absolute charging," IEEE Trans Plasma Sci.2015, 43(9):2887-2893.

- [23] Hwang CO, Mascagni M. "Electrical capacitance of the unit cube" J Appl Phys.2004, 95(7):3798-3802.
- [24] Ghosh S, Chakrabarty A., "Estimation of the capacitance of different conducting bodies by the method of rectangular subareas," J Electrost. 2008, 66(3–4):142-146.
- [25] Alad RH, Chakrabarty SB., "Electrostatic modeling of coupled metallic bodies in the shape of a funnel," Electromagnetics. 2013, 33(3):201-220.
- [26] Anju Damodaran, Joy Anil Gomes, V. B. Pramod, S. S. Kumar and V. K. Hariharan, "Microelectronics, Electromagnetics and Telecommunications, Lecture Notes in Electrical Engineering 521, 2019.
- [27] Pandya A., P. Mehta, and N. Kothari, "Impact of secondary and backscattered electron currents on absolute charging of structures used in spacecraft," Int. J. Numer. Modelling: Electron. Netw., Devices Fields, Nov. 2019, vol. 32, no. 6, Art. no. e263.
- [28] Pandya A. B, Kothari N, Alad R, Joshi R, Gupta S, Mehta P., "Secondary and backscattered electron currents induced differential charging on a triple junction of spacecraft." IEEE Trans Plasma Sci. 2020,48(4):1162–1172.
- [29] Lai ST. Spacecraft Charging. Virginia: American Institute of Aeronautics and Astronautics, Inc; 2011,1-4 19,25.
- [30] Whipple EC.," Potentials of surfaces in space," Rep Prog Phys. 1981, 44:1209-1211.
- [31] W. C. Gibson, "The Method of Moments in Electromagnetics,", Nov. 2007, New York, NY, USA: Chapman & Hall, pp. 33–48 and 255–269.
- [32] Lai ST., "Fundamental of Spacecraft Charging, Spacecraft interactions with Plasma, "2011, Princeton University Press, Princeton and Oxford, p19.
- [33] Y. Saad and M. H. Schultz, "GMRES: A generalized minimal residual algorithm for solving nonsymmetric linear systems," SIAM J. Sci. Statist. Comput., Jul. 1986, vol. 7, no. 3, pp. 856–869.
- [34] D.E. Hastings and H.B. Garrett, "Spacecraft–Environment Interactions," Cambridge, U.K.: Cambridge Univ. Press,1996, p. 20 and 148–154.
- [35] Wang S, Zhan-Cheng W, Tang X-J, Yi Z, Sun Y-W., "A new charging model for spacecraft exposeddielectric (SICCE)," IEEE Trans on Plasma Sci. 2016, 44(3):289-295.
- [36] Help: EQUIPOT Spacecraft surface charging code [online] Available:https://www.spenvis.oma.be/help/background/charging/equipot/equipot.html, accessed Jul. 1, 2023. [37] Purvis, C. K., Garrett, H. B., Whittlesey, A. C., Stevens, N. J., "Design guidelines for assessing and controlling spacecraft charging",1984, NASA TP- 2361.
- [38] Ferguson DC, Katz I. "Worst case GEO-environment and the frequency of arcs in GEO." IEEE Trans On Plasma Sci.,2015, 43(9):3021-3026.